Quantitative loss analysis of opaque perovskite solar cells using transient and steady-state characterization

Katarzyna Cudo

Faculty of Applied Physics and Mathematics, Gdańsk University of Technology, Narutowicza 11/12, Gdańsk 80-233, Poland

Riccardo Ollearo

Molecular Materials and Nanosystems and Institute for Complex Molecular Systems, Eindhoven University of Technology, P.O. Box 513, Eindhoven 5600 MB, Netherlands

Gerwin H. Gelinck

Molecular Materials and Nanosystems and Institute for Complex Molecular Systems, Eindhoven University of Technology, P.O. Box 513, Eindhoven 5600 MB, Netherlands and TNO/Holst Centre, High Tech Campus 31, Eindhoven 5656 AE, Netherlands

TNO, Materials Solutions, High Tech Campus 25, Eindhoven 5656 AE, Netherlands

Damian Glowienka **

Faculty of Applied Physics and Mathematics, Gdańsk University of Technology, Narutowicza 11/12, Gdańsk 80-233, Poland

(Received 14 May 2024; revised 17 September 2024; accepted 30 September 2024; published 8 November 2024)

Perovskite solar cells have emerged as a promising technology in the field of photovoltaics, owing to their notable advancements in power-conversion efficiency. Recent investigations have revealed a crucial dependency of efficiency on the source of bromide within the perovskite absorption layer. To elucidate the underlying nature of traps within these solar cells, a comprehensive series of measurements was conducted under varying light intensities. Subsequently, employing an electrodynamic theoretical model, the intrinsic processes inherent to caesium and lead-based perovskite solar cells with different bromide sources were analyzed. The study reveals significant differences in transient photocurrent measurements and photocurrent-voltage characteristics among perovskites originating from different bromide sources, measured under different light intensities. Leveraging theoretical analyses on the picosecond scale, the recombination mechanism of crystal defects was meticulously described revealing the pronounced influence of capture rates on electron-hole recombination dynamics. Furthermore, the investigation substantiated the presence of a band-bending phenomenon at the interface between the hole transport layer (HTL) and perovskite, elucidating the observed transient photocurrent phenomena. The findings significantly advance the understanding of the mechanisms underlying perovskite solar cells, offering valuable insights into their performance and paving the way for enhanced efficiency and stability in future device design and optimization.

DOI: 10.1103/PhysRevApplied.22.054025

I. INTRODUCTION

Perovskite solar cells (PSCs) have gained a lot of attention for a significant increase in efficiency in recent years and currently achieve 26.1% [1]. In spite of this good

Published by the American Physical Society under the terms of the Creative Commons Attribution 4.0 International license. Further distribution of this work must maintain attribution to the author(s) and the published article's title, journal citation, and DOI.

result, it is still far away from the theoretically possible efficiency of 31% [2]. This is likely caused by the nonradiative recombination process due to the imperfect nature of perovskite crystals, which directly affects the fill factor (FF) and the open-circuit voltage (V_{oc}) [3]. This is also the main reason why it is necessary to understand these mechanisms both in the bulk layer and at the interfaces.

There are a variety of techniques to partially understand the processes in PSCs [4,5]. Among the most widespread for their ability to explain the mechanisms occurring in solar cells are J-V characteristics with tuning temperature

^{*}Contact author: damian.glowienka@pg.edu.pl

or light intensity [6–17], impedance under ac signals [18], transient photocurrents [19], transient photoluminescence [20], and transient open-circuit voltage [21,22]. A common approach among various research groups is the combination of different techniques to gain a comprehensive understanding of the mechanisms occurring in solar cells.

Due to specific properties unique to PSCs, which are not typically observed in other materials [23], it is thus necessary to develop alternative analysis techniques or entirely different techniques or combinations thereof to thoroughly understand all processes occurring in PSCs. Examples of these unique properties of the PSCs are high dielectric constants, photoinduced degradation, or current-voltage (*J-V*) hysteresis effect [24–26]. Moreover, ion migration observed in perovskite materials induces the hysteresis effect and accelerates the degradation process [27–29].

Transient photocurrent (TPC) is one of the most widespread techniques [30–36] that helps to understand the nature of traps in the solar cells [37] and dominant transportation mechanisms [38]. In this method, the current response of a photovoltaic device is recorded to pulse steps (off-on-off) while being measured at constant offset voltage. In order to obtain more information about the mechanisms taking place in the devices, TPC is performed with variations of pulse in the form of light intensity, light spectra, or biased voltage [19,39]. Despite the fact that the technique is fast, inexpensive and nondestructive [40] it is not perfect and cannot be used in every case. It is restricted to the cases, when the short-circuit carrier losses are insignificant and can be ignored [4,19]. Thus, in this work, we expand this technique to use it with different light illuminations and at dc bias.

However, this technique itself cannot describe all effects occurring in the solar cells. Therefore, it is often necessary to combine transient photocurrent with other characterization techniques [40–42]. To better understand the recombination and transportation mechanisms in this work we have combined this technique with our previously reported modulated light intensity J-V characterization technique for PSCs [7]. This study simultaneously employs TPC and steady-state J-V characterization under varying light intensities, integrated with drift-diffusion electrical modeling, to explore the dominant loss mechanisms in PSCs.

We utilize our previously reported method of perovskite precursor preparation using different bromide sources [caesium bromide (CsBr) or lead bromide (PbBr₂)] in the same perovskite structure [43]. In our previous work, we have extensively reported on these bromide sources, including their morphological and structural characteristics. Consequently, our focus here is on exploring electrical mechanisms using this technique to manipulate recombination and transport processes in PSCs. The experimental results are supported by the electrical modeling that was used to simulate all experimental variations with one set of parameters.

II. RESULTS AND DISCUSSION

The dual cation (2C) perovskite with the structure of Cs_{0.18}FA_{0.82}Pb(I_{0.94}Br_{0.06})₃ was synthesized using CsBr and PbBr₂ as sources of bromide to prepare the perovskite precursor, following a method previously reported [43]. The studied PSCs were fabricated with the following architecture glass/ITO/PTAA/2C perovskite/PCBM/BCP/Cu. The devices with a perovskite absorber layer using CsBr and PbBr2 are referred to as Cs-Br and Pb-Br, respectively. We employed the same manufacturing technique for the PSCs as in our previous report [43]. Both examined PSCs were characterized using a sun simulator, with light intensities ranging from 0.0001 to 1 suns. Figure S7 within the Supplemental Material [44] shows the statistical distribution of the photovoltaic parameters for both types of samples. PSCs demonstrate high reproducibility with PCE equal to $16.96\% \pm 0.34\%$ for Cs-Br samples and $10.33\% \pm 0.49\%$ for Pb-Br samples. Similarly, light-intensity studies are presented for four independent devices, demonstrating the negligible effect of statistical variation for Cs-Br and Pb-Br samples, as shown in Figs. S8 and S9 within the Supplemental Material [44], respectively. Additionally, all samples exhibit a negligible hysteresis effect with stable maximum-power-point (MPP) tracking, see Figs. S7 and S10 (Supplemental Material [44]).

Figure 1 shows the photovoltaic parameters for both representative samples of Cs-Br and Pb-Br PSCs, including both experimental and simulation results. Figure 1(a) illustrates the variation of power-conversion efficiency (PCE) with light intensity. In the Cs-Br sample, PCE decreases linearly from 17.35% to 8.58%. Conversely, the Pb-Br sample exhibits a slight increase in PCE followed by a drop from 10.90% to 5.03%. The linear trend of shortcircuit photocurrent (J_{sc}) is evident in the log-log scale, shown in Fig. 1(b), where both samples exhibit the same slope equal to 1. Confirmation of J_{sc} at 21.4 mA cm⁻² is achieved through external quantum efficiency (EQE) measurements, yielding a value of 20.14 mA cm⁻², as shown in Fig. S11A (Supplemental Material [44]). Additionally, EQE measurements determine the band gap of the perovskite to be 1.56 eV, as illustrated in Fig. S11B within the Supplemental Material [44]. However, the Pb-Br sample has $J_{\rm sc}$ lower by 1.36 mA cm⁻². The major differences in the operation of PSCs are clearly visible in fill-factor (FF) and open-circuit voltage (V_{oc}) across a wide range of light intensities. The peak FF for Cs-Br is 73%, which is 17% less than Shockley-Queisser (SQ) limit value [see Fig. 1(c)]. FF does not diverge significantly from the peak FF in high light intensities. In contrast, the Pb-Br PSC sample exhibits a peak FF equal to 71%, which is 19% lower than the SQ limit. For high light intensity, there is a relevant drop of the FF to the value of 55%. Whereas, for low light intensities, it drops down to around 59%. In

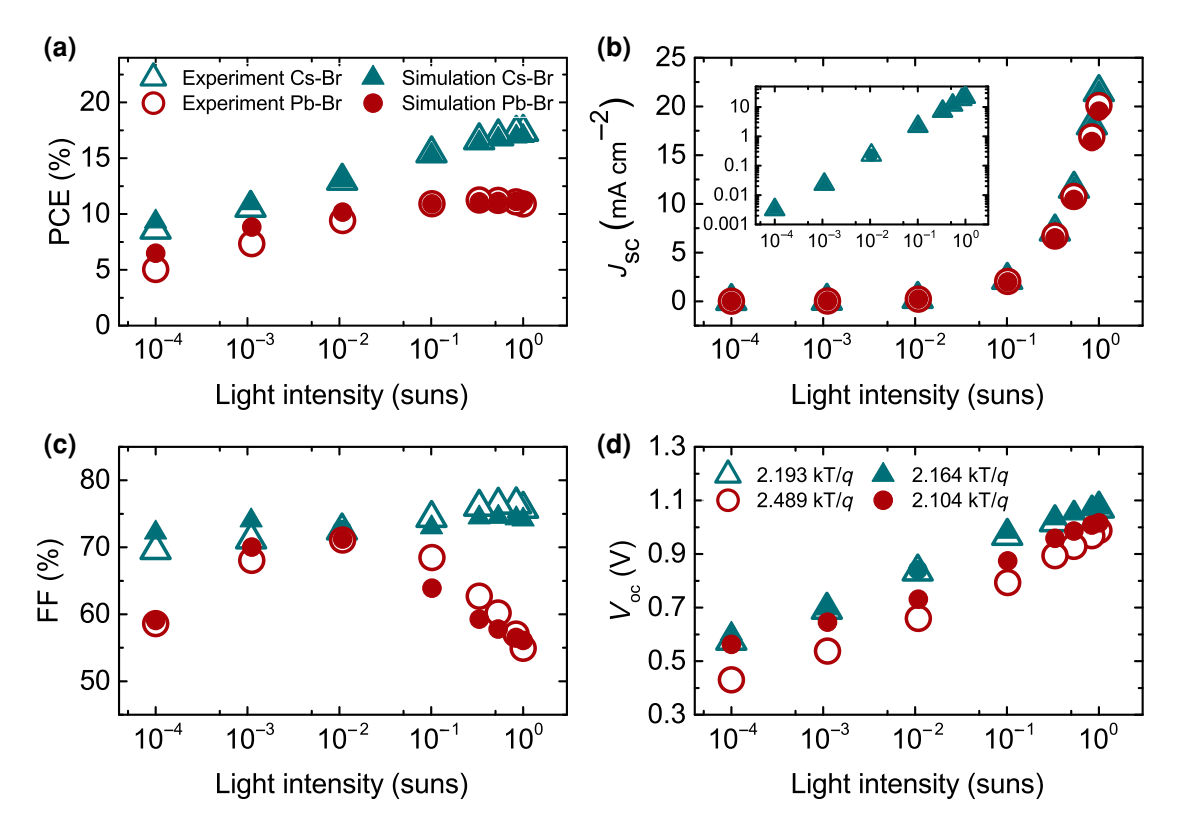


FIG. 1. Photovoltaic experimental (open symbols) and simulation (full symbols) photovoltaic parameters of (a) PCE, (b) J_{sc} , (c) FF, and (d) V_{oc} in the function of light intensity for PSCs with Cs-Br (blue) and Pb-Br (red). The inset of (b) shows log-log scale of J_{sc} for the experimental and simulation results.

Fig. 1(d), it is evident that across the entire spectrum of light-intensity data, $V_{\rm oc}$ is approximately 60 mV higher for Cs-Br PSCs. The ideality factor ($n_{\rm id}$) for experimental results is quite similar for both types of solar cells and it is slightly over 2. The modulated light-intensity analysis reveals three key observations: (1) the interface losses are higher in the Pb-Br sample, resulting in severe reduction in both FF and $V_{\rm oc}$ by 20% and 80 mV, respectively, at high light intensities; (2) bulk trap-assisted recombination show minimal difference, as indicated by the peak FF observed in both PSCs; (3) observable losses occur in low light intensity for the Pb-Br sample compared to Cs-Br PSC, suggesting the appearance of the shunt resistance.

Figures S1 and S2 within the Supplemental Material [44] show the simulation and experimental *J-V* characteristics altogether. The simulation of both Cs-Br and Pb-Br has been fitted with a goodness of fit of 96% and 14%, respectively. The goodness of fit is calculated in respect to every point in the function of light intensity. Consequently, matching such a complicated function poses significant challenges, and as a result some parts of the *J-V* characteristics for Pb-Br PSCs are not aligned perfectly. This discrepancy is primarily attributed to the S-shape behavior observed in the *J-V* characteristic for the Pb-Br sample [45]. There are two possible mechanisms

that can cause the curve to flatten, appearing either above OC or around the maximum-power-point (MPP). The first mechanism typically occurs when the transport properties of the layer are very poor, causing the film to behave like an insulator layer. However, recent studies have shown that it might also appear at MPP as a consequence of high interface recombination and charge-carrier accumulation at the perovskite/PCBM interface [46]. The simulation parameters for all the layers in PSCs used in the electrical modeling are given in Table S1 (Supplemental Material [44]).

The main modeling parameters for the Cs-Br and Pb-Br samples are shown in Table I. Firstly, it can be observed that there is a small difference in the mobility of charge carriers for two types of PSCs. As has been already shown, the value of charge-carrier mobility differs a lot when measured from sample to sample [47]. Therefore, the small deviation that has been observed can be considered as a negligible measurement error. When analyzing the Cs-Br sample, it is quite interesting to observe that the sample-dominant interface loss mechanisms is located at the perovskite/ETL interlayer, which is more than 20 times more defective than the HTL/perovskite interface. However, the opposite relation is being observed for the Pb-Br sample, where the HTL/perovskite boundary is around 40

TABLE I. List of perovskite-layer parameters deviating from the reference used in the simulation of the Cs-Br and Pb-Br PSCs. Parameters for holes are in the bracket.

Name	Parameter	Unit	Cs-Br	Pb-Br
Mobility	$\mu_{n(p)}$	$10^{-3} \text{ cm}^2 \text{ V}^{-1} \text{ s}^{-1}$	1.74	1.31
HTL interface trap density	$N_{\mathrm{tc}(v)}$	$10^{21} \ \mathrm{m}^{-3}$	28	5910
Bulk trap density		$10^{21} \ \mathrm{m}^{-3}$	3	19
ETL interface trap density		$10^{21} \ \mathrm{m}^{-3}$	722	145
Band bending		meV	0	128
Shunt resistance	$R_{ m sh}$	$\Omega~{ m m}^2$	∞	95
Bulk capture rate rate in the conduction band for electrons	$C_{ m nc}$	$10^{-14} \text{ m}^3 \text{ s}^{-1}$	2	0.37
Bulk capture rate in the valence band for electrons	$C_{ m nv}$	$10^{-14} \text{ m}^3 \text{ s}^{-1}$	2	0.02
Bulk capture rate in the valence band for holes	C_{pv}	$10^{-14} \text{ m}^3 \text{ s}^{-1}$	2	0.9
HTL interface capture rate in the conduction band for electrons	$C_{ m nc}$	$10^{-14} \text{ m}^3 \text{ s}^{-1}$	2	0.02

times more defective. Due to the extremely large interface recombination and high bulk recombination in the Pb-Br PSC, we can assume that the ETL/perovskite interface is being underestimated. Most likely, the recombination for the Pb-Br sample from the ETL side is similar to the Cs-Br PSC. Based on the simulation results, it can be observed that the density of trap states at the HTL/perovskite and bulk of the perovskite layer of the Pb-Br sample is around 6 and 200 times higher than in the Cs-Br PSC, respectively. That clearly shows the domination of the nonradiative recombination process in the Pb-Br sample. Furthermore, the simulation has shown the best experimental match if including the band-bending process at the HTL/perovskite interface. We have already shown the presence of such a process on both of the interfaces in the PSCs [46,48]. It is especially interesting that such a presence of the process very often happens in PSCs together with the extremely high interface recombination, which altogether appears as an S shape of the J-V characteristics. Based on these results, it can be concluded that the dominant processes in the Pb-Br occur at the HTL/perovskite interface.

One of the main issues with the understanding of the dominant loss mechanism in PSCs is to determine the dominant recombination interface. In the case of perovskite material, this is mainly due to extremely high diffusion length, which allows for diffusion of free charge carrier from one side to the other if the recombination is not extremely dominant [49]. Therefore, using the electrical simulation tool, we need at least several J-V characteristics in different operational conditions like light spectra, light intensity, or temperature to define the dominant defect recombination side. We have already shown that for semitransparent PSCs it is possible once measuring on both sides [7]. However, the difficulty arises, when analyzing opaque devices. Therefore, here we additionally investigated a monochromatic light source with 543.5-nm wavelength using transient photocurrent (TPC) analysis on the same studied devices.

Figure S3 within the Supplemental Material [44] shows the TPC results for the Cs-Br sample. Parts A and B

show the tendency under different biases with 0 and 0.6 V, respectively. It can be clearly observed that there are negligible differences and an almost perfect plateau on the illuminated period of measurements. This kind of flat curve behavior is well known to appear for samples with high transportation properties [50]. The rising time increases linearly from 43 to 52 μ s, and also from 34 to 41 μ s for unbiased (Fig. S3A within the Supplemental Material [44]) and biased (Fig. S3B within the Supplemental Material [44]) conditions with lowering the light intensity, respectively. However, this seems to be mostly generated from the parasitic capacitance that might appear due to a nonideal connection from the measurement system. This clearly explains the slight decrease in the rising time for the biased sample. The simulation results follow exactly the same tendencies for both unbiased and biased measurements. The Cs-Br PSC has been simulated using the same electrical modeling as for the steady-state conditions, except for the parasitic capacity, which for simplicity is used only in transient simulations. The value is equal to 6 mF m². However, the fit matches very well with the experimental simulations, we have noticed that parasitic capacitance might be slightly higher for the Cs-Br sample. For simplicity, we have kept the same values for all the transient simulations presented in the paper.

The waveform of TPC for the Pb-Br sample, measured without applied voltage, is also close to the ideal rectangular shape, see Fig. 2(a). The same shape is observed regardless of the laser. The rising time increases linearly with the irradiation power from 63 to 107 μs for an unbiased sample. However, it is especially interesting that when a higher voltage is applied, the shape of the TPC measurement for the Pb-Br sample changes dramatically. This is particularly noticeable in high light intensity, see Fig. 2(b). We observe an extremely high peak in photocurrent just after illuminating the sample. To reach the maximum photocurrent it takes a very short time of around 20 to 30 μs with lowering the light intensity. Also, the width of the peak is increasing linearly with the decrease of light intensity. Furthermore, at the lowest laser power, the shape of the characteristic again

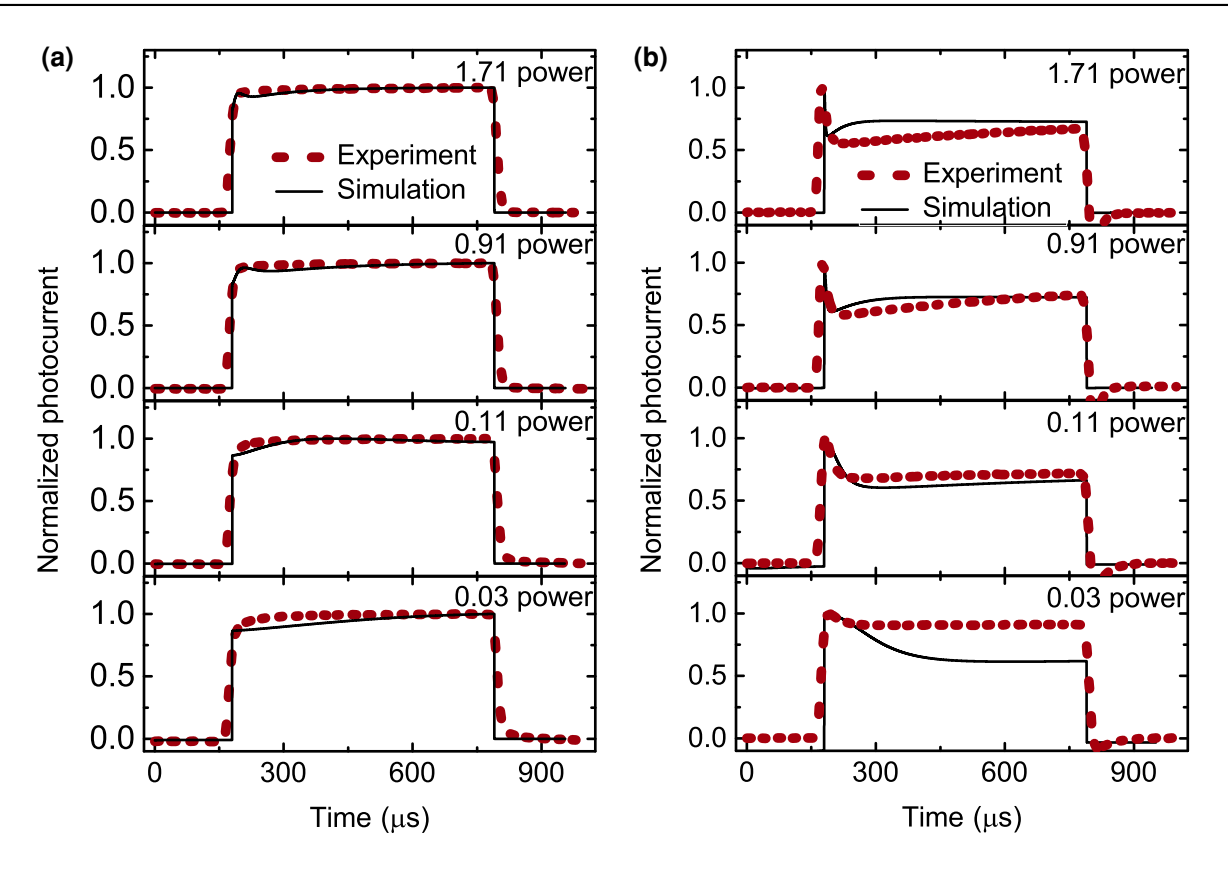


FIG. 2. Transient photocurrent for Pb-Br PSC at (a) 0.0 V, and (b) 0.6 V applied voltage.

starts to plateau without any peak. This behavior has two very useful characteristics. Firstly, it appears only when the bias is getting closer to OC conditions, and secondly it disappears with lower laser illumination. Thus, the mechanism is clearly related to the recombination process, which always dominates under OC conditions. Also, it seems to be an interfacial effect since, it is related to the high photon flux that results in high charge-carrier concentration.

The simulation results are done using all the same parameters as in the steady-state condition for the Pb-Br sample, see Table I. The results clearly follow the experimental trends. The simulation results reproduce exactly the rise and the width of the peak at the highest laser power for 0.6-V biased measurements. However, for the lowest light intensity, the observable mismatch could be found between the experimental and simulation results. It should be noted that the measured peak of photocurrent disappears slightly faster and becomes a squarelike shape if compared to the best match of simulation results. It means that the value of the mechanism has been slightly overestimated, which is especially visible at the lowest laser power. Also, it is worthwhile to note that since the experiment has been done in two separate equipment, it might be possible that the sample has slightly changed over the time between measurements. Therefore, it might not be possible to match all experimental results with one set of parameters.

It has been found that the critical parameters responsible for the behavior of the TPC results in the Pb-Br sample is the capture rate in the conduction and valence band in the bulk of perovskite film. It is nearly 2 to 10 times lower for the Pb-Br sample if compared to Cs-Br simulation results. The value of the HTL/perovskite interface capture rate in the conduction band for electrons is 10 times lower for Pb-Br than for Cs-Br PSC. It is worth mentioning that the values would not be found from only the steady-state simulations since the capturing rates would be simply replaced with simpler stationary recombination mechanism. Thus proving the need for a simultaneous fit of both transient and steady-state measurement techniques. Therefore, it can be concluded that in the Pb-Br sample we have the set of following mechanisms that explain all experimental observations: (1) at the HTL/perovskite interface there is an observed band-bending effect that results in the accumulation of the charge carriers, which lead to a very high but slower nonradiative recombination process, (2) the bulk is more severely defected once using the PbBr2 compound, and also the recombination capturing and decapturing rates are leading to a nonstable rise of photocurrent similar to the charging of the capacitor mechanism. Therefore, the combination of the bulk and HTL/perovskite defect recombination mechanism and the band bending are responsible for the appearance of the characteristic peak in the TPC

measurements. However, the same mechanism is simultaneously responsible for the steady-state observations of S shape in the J-V characteristic, which leads to a major loss of FF at high light intensity.

In order to better understand the mechanisms responsible for the characteristic points in the TPC analysis we focus on the spatial simulation results, see Fig. 3. Based on the previous analysis, we have chosen six characteristic points for the Cs-Br and Pb-Br samples measured at the highest laser power and 0.6-V bias, where the effects are most strongly visible. For clarity, one might refer to Fig. 3 to look at the specific TPC analysis points for Cs-Br PSC [A to C; Fig. 3(a)], and also for Pb-Br [D to F; Fig. 3(b)] sample. The energy diagram in the Cs-Br sample has shown a very flat energy diagram, especially for quasi-Fermi levels in the dark conditions (A point), as shown in Fig. 3(c). For B point, the light is on and there is a natural shift in quasi-Fermi levels in the absorber layer. This visibly affects the spatial photocurrent distribution, which acts very symmetrically for both electrons and holes, see Fig. 3(d). There is a very small shift in energy level from points B to C, which is related to a short time of around 20 µs during sample illumination. This is slightly affecting the photocurrent distribution to achieve steady-state conditions. Figure 3(e) shows the Pb-Br energy-level diagrams for D to F characteristic TPC points. This time all three points are shown for the illumination conditions. Firstly, the photocurrent peak in the Pb-Br sample has a much higher quasi-Fermi-level splitting, which is equal to around 0.9 eV. Whereas 0.6 eV is strongly related to applied bias, and the other 0.3 eV directly comes from the band-bending effect. This mechanism changes the conduction and valence band alignment by lowering energy levels and reducing the energy pinning effect. This is opposite to the normal operation of PSC without band bending, as shown in Fig. 3(c). It directly impacts the spatial photocurrent distribution for the Pb-Br sample, see Fig. 3(f). The HTL/perovskite interface limits charge-carrier extraction to the electrode. This lowers the total photocurrent generation from the device. Also, the photocurrent peak value (D point) is mostly due to the initial rise of photocurrent in the bulk of perovskite film. Similarly in the next characteristic time point (E) the hole and electron photocurrents are lost at the bulk of the perovskite layer due to the energy-level change of the conduction and valence band that follows the direction of the band-bending energy alignment. At last, the small amount of photocurrent increases, when the steady-state condition is reached during the illumination (F point). A similar mechanism is observed in all light intensities under 0.6-V bias but for the sake of simplicity we do not show the results here.

Once the detailed mechanism is well clarified, the detailed electrical loss analysis technique can be applied to quantitatively define the FF and $V_{\rm oc}$ from the proposed processes. Such a methodology can easily lead to defining

TABLE II. Summary of the FF and $V_{\rm oc}$ losses for Cs-Br and Pb-Br samples.

	Cs	Cs-Br PSC		Pb-Br PSC		
	FF	$V_{\rm oc}$	FF	$V_{\rm oc}$		
HTL/perovskite	2%	20 mV	25%	120 mV		
Bulk perovskite	6%	154 mV	4%	181 mV		
Perovskite/ETL	7%	60 mV	6%	20 mV		

the optimization strategies, which is extremely useful in the optimization of PSCs [48]. Figure S4 within the Supplemental Material [44] shows the ideal diode model without electrical losses in the form of transportation or nonradiative recombination. Therefore, it is only limited by the radiative recombination, similar to the Shockley-Quisser limit calculations. However, the optical loss analysis is not included in the paper. For also that reason, we further focus only on FF and $V_{\rm oc}$ losses since the transportation and recombination processes are dominating MPP and OC conditions. Figure S4C, within the Supplemental Material [44], shows the FF of around 90% for ideal PSC without bulk and interface recombination and transportation losses. We have kept the energetical interfaces and mobility of charge carriers in all layers but removed the HTL, ETL, and bulk recombination. Since the transportation and recombination are strictly connected, when there is no recombination the transportation losses also do not appear. Similarly, the $V_{\rm oc}$ for the ideal diode with 1.58-eV band gap gives around 1.3 V being limited by only radiative recombination, see Fig. S4D (Supplemental Material [44]).

Figure 4 shows the electrical loss analysis for the Cs-Br sample. Three variations of the bulk, HTL/perovskite, and perovskite/ETL defect densities are calculated. Thus, following the values from Table I and using the previously calculated ideal diode model results we can clearly calculate the electrical losses for the Cs-Br device. Table II provides a summary of FF and V_{oc} losses associated with both the interfaces and bulk nonradiative recombination processes. Therefore, the perovskite/ETL interface defects lead to a loss of FF and $V_{\rm oc}$ equal to 7% and 60 mV, respectively. From the other HTL/perovskite interface nonradiative recombination we found loss of FF equal to 2% and $V_{\rm oc}$ up to 20 mV. Similarly, the bulk defects of the perovskite layer lead to 6% and 154 mV losses of FF and $V_{\rm oc}$, respectively. Meaning, that totally, we loss 15% of FF and 234 mV of $V_{\rm oc}$ for the Cs-Br sample if comparing to theoretical radiative limit.

The loss analysis of Pb-Br PSC is shown in Fig. 5. The same procedure has been used, however here we also include the band-bending process at the HTL/perovskite interface. It is worthwhile to mention that if the Pb-Br sample has no band-bending effect and no nonradiative recombination losses, then the device becomes limited

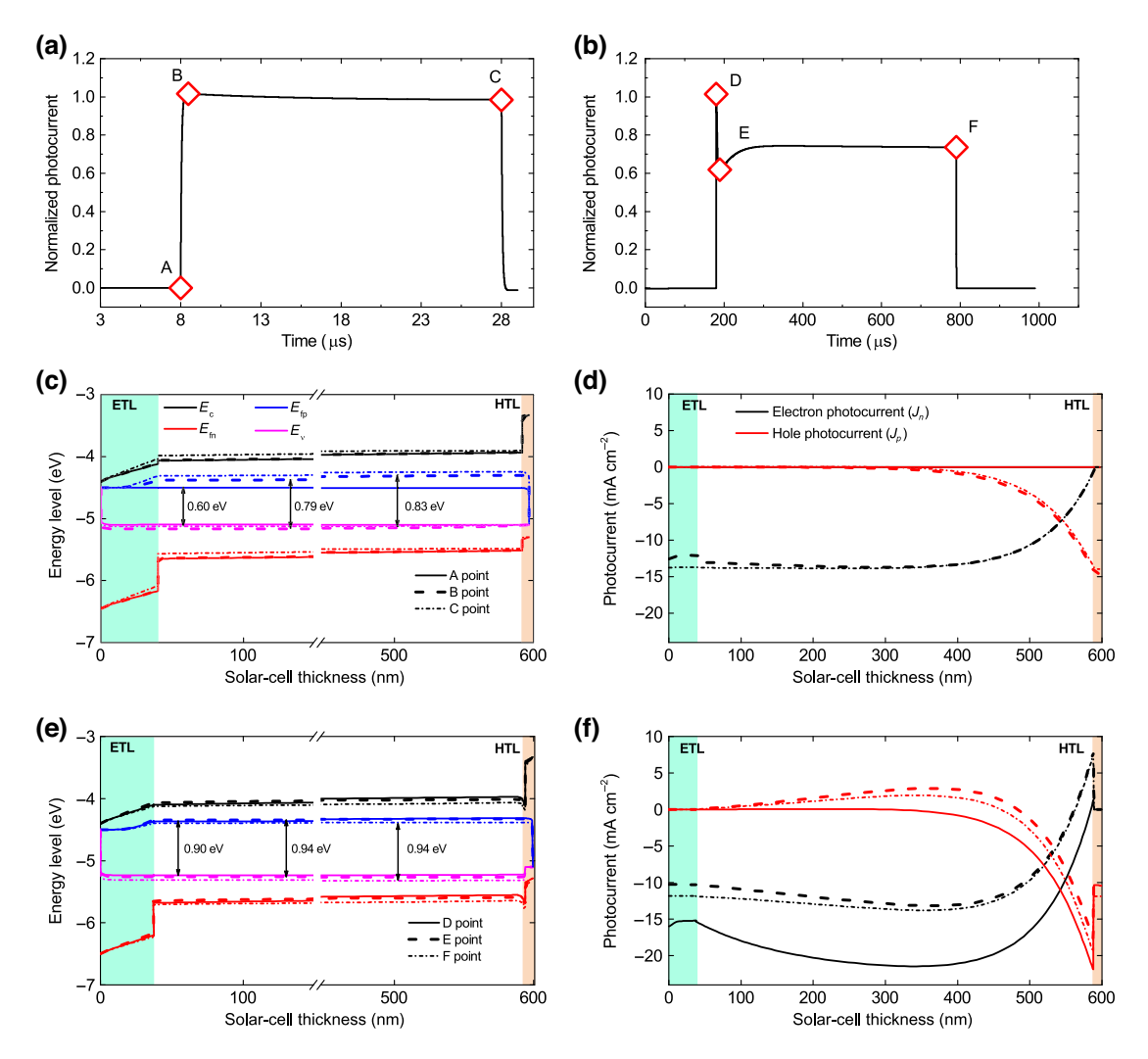


FIG. 3. Transient photocurrent for (a) Cs-Br, and (b) Pb-Br PSC to show the characteristic points (red closed squares) in the TPC analysis used for transient simulations. Spatial analysis spatial energy-level diagrams and electron (or hole) photocurrents of TPC simulation results for Cs-Br (c), (d), and for Pb-Br (e), (f) samples. The results are presented for characteristic points for Cs-Br at A to C points. Similarly, for the Pb-Br sample at D to F points.

by radiative recombination only. Meaning, we shall also calculate the additional transportation losses by including the band-bending mechanism. Table II details all losses in photovoltaic parameters associated with parasitic mechanisms. Therefore, the perovskite/ETL interface leads to only 6% and 20 mV of FF and Voc loss, respectively. It is quite similar to the case of the previous sample but with lower $V_{\rm oc}$ losses. It is mostly due to higher domination of the HTL/perovskite interface mechanism in the case of Pb-Br PSC. At this interface we have found losses as high as 25% of FF and 120 mV of $V_{\rm oc}$. This strongly supports the previous observations and shows the extreme domination of the HTL/perovskite interface. At last, the bulk nonradiative processes are leading to the loss of 4% of FF and 181 mV of $V_{\rm oc}$. This mostly influences the $V_{\rm oc}$ losses if comparing to the Cs-Br sample since the value of bulk defect recombination is much higher. In total, the Pb-Br device loses 35% of FF and 321 mV of $V_{\rm oc}$.

We have already shown that the TPC simulations are mostly affected by the bulk nonradiative capturing rate in the conduction band for electrons ($C_{\rm nc}$) of the perovskite layer. Similarly, the other capture and decapture rates were also checked on the perovskite/ETL and HTL/perovskite interfaces but it has shown a negligible effect on the TPC simulation results. Therefore, we have only calculated the variation of the $C_{\rm nc}$ parameter for the steady-state and transient simulations, see Fig. 6. The steady-state simulation shows a clear drop of PCE in the whole range of light illumination for higher $C_{\rm nc}$ parameters, as shown in Fig. 6(a). The drop is not related to the $J_{\rm sc}$ [see Fig. 6(b)] losses but rather a clear drop of FF, see Fig. 6(c). This is clearly observed as a decrease in the peak FF, which is always attributed to the bulk defect recombination and

somehow always located in around 10^{-2} suns [7]. Therefore, it would be expected to observe a similar effect from the $C_{\rm nc}$ parameter. Also, it slightly influences the ideality factor ($n_{\rm id}$) with a linear increase in the capturing rate. This is mostly due to the drop of $V_{\rm oc}$ at the low light intensity. This stays in agreement with the previous experimental observations. Also it is clearly related to the domination of the bulk of the perovskite layer, which always leads to higher $n_{\rm id}$ [51].

The impact on the TPC results is clearly observed in Fig. 6(e). The effect of the $C_{\rm nc}$ in the bulk of the perovskite layer is visible for both high and low laser power. For the $C_{\rm nc}$ value the TPC simulation results are almost identical to the measurements without bias. Meaning it appears to be the square shape of photocurrent in time function.

However, for higher values, it affects the peak height and width of the TPC simulations. It is especially visible in the lower laser power, where photocurrent decreases, and also stabilizes in a longer time.

III. SUMMARY

This paper presents an analysis of the mechanisms occurring in dual-cation PSCs, using two salts as a source of bromide: the caesium bromide and lead bromide. The experimental results indicated that Cs-Br PSC exhibited significantly higher efficiency compared with Pb-Br devices. During the steady-state simulations it was observed that in the Cs-Br sample most of the observed losses are concentrated at the perovskite/ETL interface. In

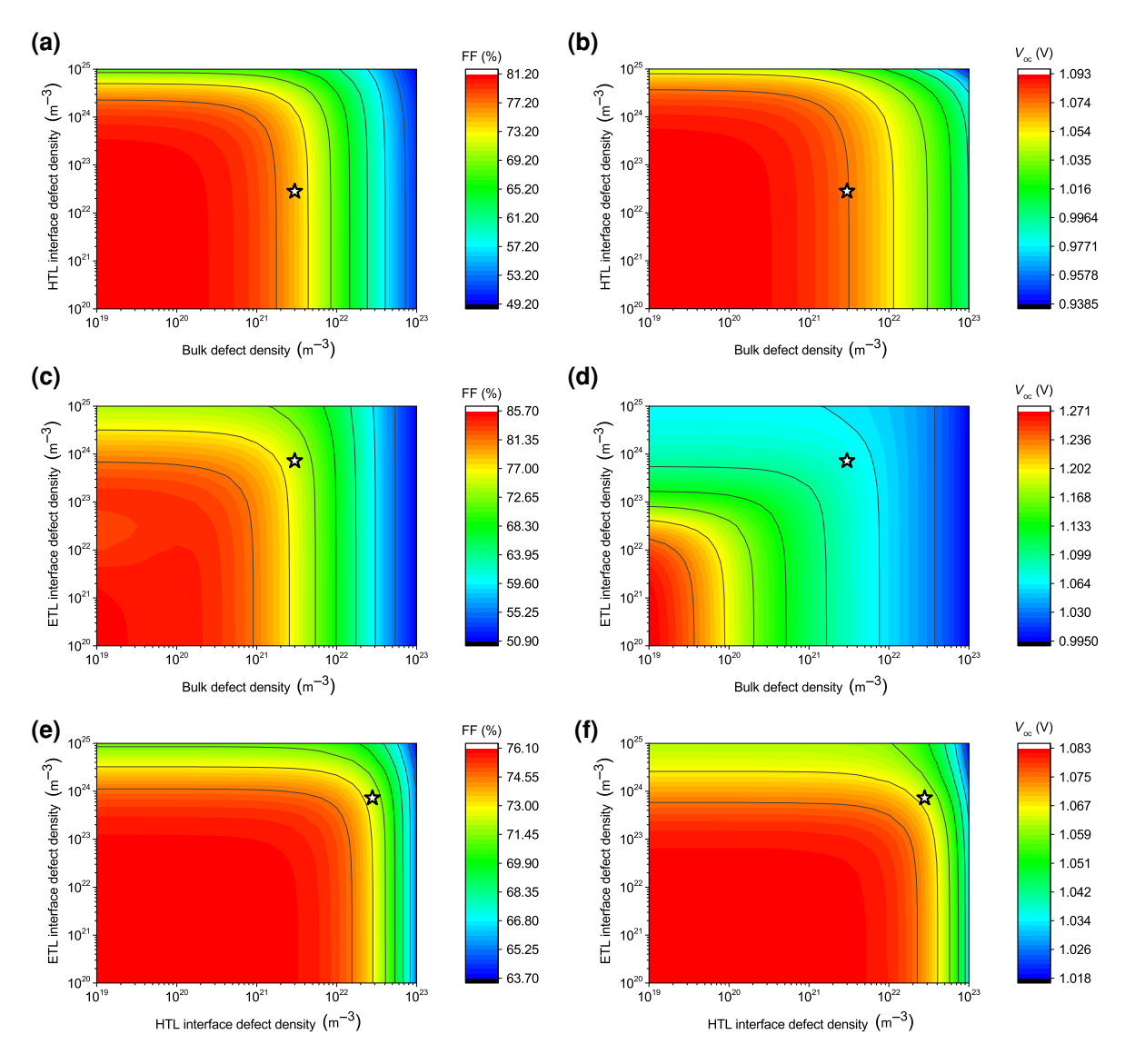


FIG. 4. Simulated results of 3D graphs of light-intensity-dependent (a), (c), (e) FF and (b), (d), (f) V_{oc} considering different levels of bulk and interface defect densities, responsible for bulk and interface recombination. (a), (b) HTL/perovskite-bulk, (c), (d) perovskite/ETL-bulk, (e), (f) perovskite/ETL-HTL/perovskite for the Cs-Br sample.

contrast, for the Pb-Br sample, the main reason for the high losses was attributed to the HTL/perovskite interface. Moreover, at this interface in the Pb-Br solar cell, a band-bending process was discovered along with the defect concentration approximately 6 times higher than that in the Cs-Br PSC. It was also observed that the density of trap states in the bulk of the perovskite layer was several times higher for the Pb-Br sample compared to Cs-Br PSC. These processes contribute to a significant loss of FF, resulting in the formation of an S shape in the J-V characteristic and ultimately lowering the value of the efficiency. The ETL/perovskite interface was found to have a nonsignificant role in the dominant mechanisms observed in the Pb-Br sample. During TPC simulations it was found that the observed photocurrent peak resulted from a combination of processes at the HTL/perovskite interface and the bulk defect recombination mechanism in the perovskite layer. Additionally, besides the mechanisms affecting the steady-state simulations, a critical effect of the nonradiative capturing rate in the conduction band for electrons of the perovskite layer was identified. This factor was found to be crucial for the fitting of the width, height, and shape of the peak in the TPC measurement.

In summary, our results extends the conclusion from our previous reports by highlighting that PSCs prepared with PbBr₂ salt exhibit a higher concentration of the defects. Additionally, it has also been observed that the nature of the dominant process is evident not only under the steady-state conditions, but also in the transient measurements. Our in-depth analysis of the processes in PSCs with different bromide sources has identified and quantitatively determined the dominant loss channel. This discovery presents a

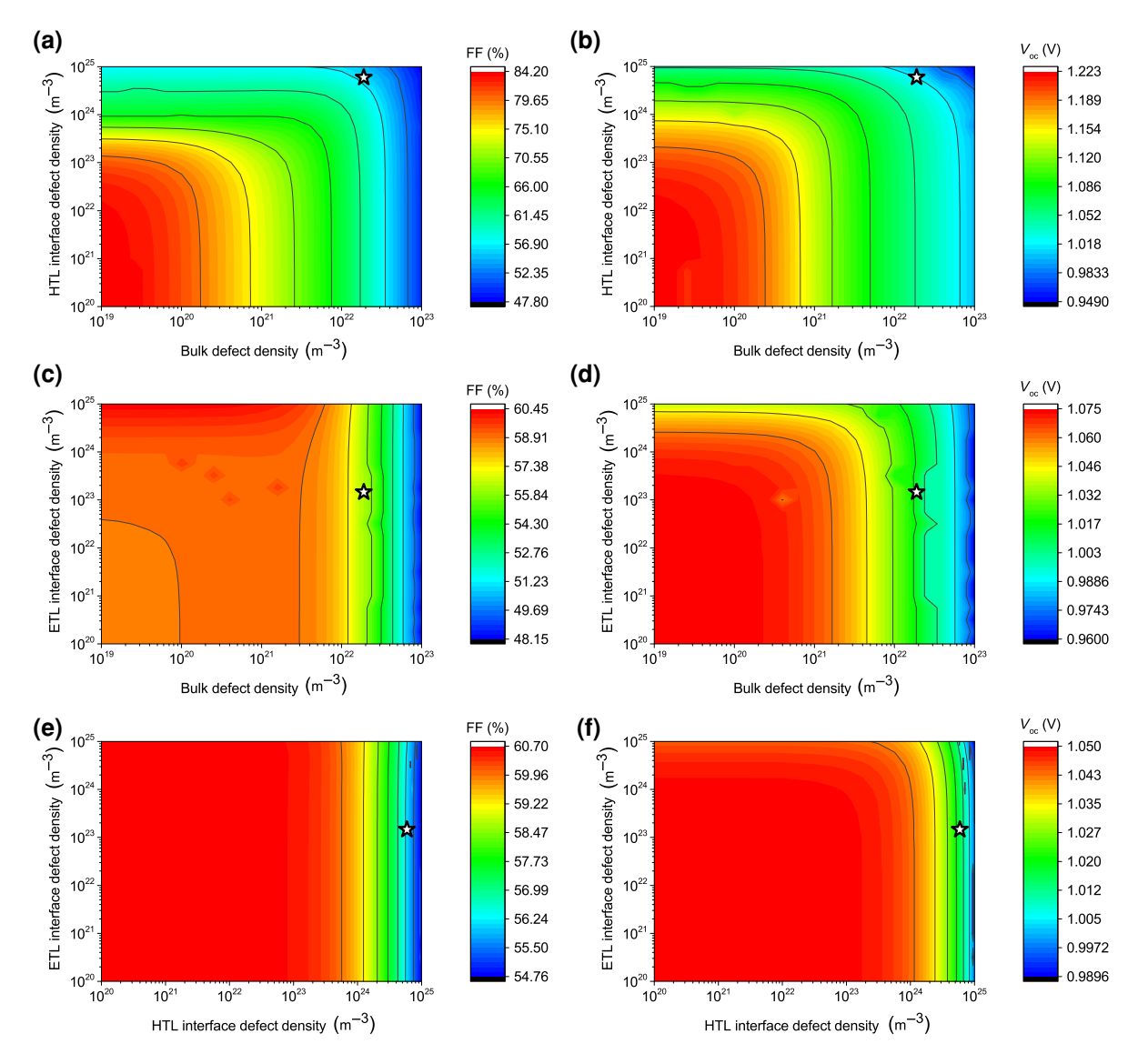


FIG. 5. Simulated results of 3D graphs of light-intensity-dependent (a), (c), (e) FF and (b), (d), (f) V_{oc} considering different levels of bulk and interface defect densities, responsible for bulk and interface recombination. (a), (b) HTL/perovskite-bulk, (c), (d) perovskite/ETL-bulk, (e), (f) perovskite/ETL-HTL/perovskite for the Pb-Br sample.

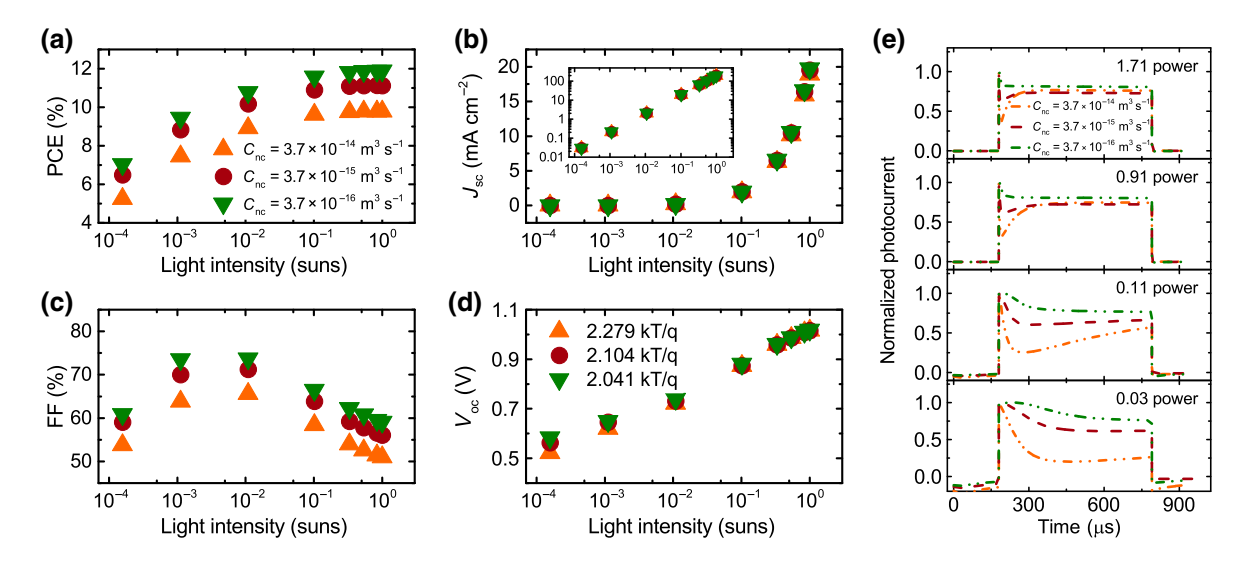


FIG. 6. Influence of capture rate in the conduction band for electrons at 0.6-V applied voltage on photovoltaic parameters for PSC with Pb-Br, (a) PCE, (b) J_{sc} , (c) FF, and (d) V_{oc} , and also (e) photocurrent in time function for PSC with Pb-Br.

potential optimization strategy to further enhance the PCE of hybrid solar cells. Moreover, the conducted research contributes to the possibility of better and faster analyses of solar-cell processes by understanding steady-state J-V characterization together with transient photocurrent measurements under varying light intensities.

IV. EXPERIMENTAL SECTION

The perovskite for the $Cs_{0.18}FA_{0.82}Pb(I_{0.94}Br_{0.06})_3$ precursors were prepared as follows. Commercial lead iodide (PbI₂) (99.99%, TCI), formamidinium iodide (FAI) (GreatCell Solar), caesium iodide (CsI) (99.999%, Sigma-Aldrich), lead bromide (PbBr₂) (99%, TCI), formamidinium bromide (FABr) (GreatCell Solar), caesium bromide (CsBr) (99.999%, Alfa Aesar), dimethylformamide (DMF) solvent (99.8%, Sigma-Aldrich), and 1methyl-2-pyrrolidinone (NMP) solvent (99.5%, ACROS Organics) were used without further purification. Two perovskite materials were prepared, here called Pb-Br and Cs-Br considering only the single bromide source. Pb-Br was obtained by mixing 1.2 M PbI₂, 1.1 M FAI, 0.24 M CsI, and 0.12 M PbBr₂ powders. Cs-Br was also produced by adding together 1.33 M PbI2, 1.1 M FAI, and 0.24 M CsBr. The perovskite powders were dissolved in DMF/NMP solvent mixture (9:1 volume ratio) and stirred at least overnight at room temperature.

The patterned glass/ITO substrates were cleaned using ultrasonication and also followed with the UV-ozone treatment for 30 min. All the preparation processes of the PSCs were done in the glovebox with an N_2 environment. The oxygen and moisture levels were always kept at about the level of 1 ppm. The hole-transporting layer (HTL) was spin coated with 2 mg ml⁻¹ solution in toluene of poly(triaryl amine) (PTAA) (Sigma-Aldrich) at speed

equal to 5000 rpm for 35 s and the acceleration equal to a 5000 rpm s^{-1} . The sample with the PTAA layer was annealed at 100 °C for 10 min. The perovskite solution was dynamically spin coated using the gas-quenching technique [52]. The two-step spin-coating program was used to obtain the desired thickness. Firstly at 2000 rpm for 10 s and with 200 rpm s⁻¹ acceleration, and secondly at 5000 rpm for 30 s with 2000 rpm s^{-1} . The quenching process was done using a nitrogen gun after 15 s of spin coating in the second step and it was kept for another 15 s at 6 bars of pressure with a 10-cm vertical distance from the sample. The perovskite samples were further placed on the hot plate with 100 °C for 10 min. The electrontransporting layer (ETL) solution with 20 mg ml⁻¹ concentration was made using [6,6]-phenyl C61 butyric acid methyl ester (PCBM) (99%, Solenne) material dissolved in chlorobenzene. The solution was always kept stirring overnight at 60 °C. The solution was spin coated dynamically with a speed of 1500 rpm for 55 s and acceleration equal to 3000 rpm s⁻¹. The buffer layer was spin coated with 0.5 mg ml⁻¹ bathocuproine (BCP) (99.99%, Sigma-Aldrich) solution in ethanol with 3000 rpm for 50 s and 3000 rpm s⁻¹. Subsequently, the cleaning of ITO contacts was done in the air with DMF and chlorobenzene solution in a 1:6 volumetric ratio. Finally, 100-nm gold electrodes were thermally evaporated using shadow masks placed on top of the samples. The deposition was accomplished under a vacuum pressure not higher than 1×10^{-6} mbar.

The photocurrent-voltage (J-V) characteristics of PSCs were measured in the glovebox with N_2 environment using Keithley 2400. The samples were illuminated under a white-light halogen lamp and using the illumination mask to define the active area equal to 0.09 cm². The light irradiance of 1 sun was calibrated to 100 mW cm⁻²

with a silicon reference cell. To apply the light-intensitymodulated technique, a set of filters was used to obtain 0.83, 0.53, 0.33, 0.1, 0.01, and 0.001 suns. The light irradiance, equivalent to 1 sun, was calibrated to 100 mW cm⁻² using a silicon reference cell, and similar calibrations were applied to other sunlight intensities. The specified light intensities were achieved using the following set of filters: ND01, ND03, ND05, ND10, ND20, and ND30. To apply the light-intensity-modulated technique, a set of filters was used to obtain 1, 0.83, 0.53, 0.33, 0.1, 0.01, and 0.001 suns. The measurements for light-intensity analysis are done only for reverse scan. The J-V characteristics were measured using a scanning rate equal to 0.165 V s⁻¹ with 20-mV step. The measurements were performed in the reverse (from 1.1 to -0.1 V) and forward (from -0.1 to 1.1V) scanning directions to observe the hysteresis effect. The preconditioning was achieving under MPP tracking for 2 min under 1-sun conditions. The transient photocurrent (TPC) measurements were performed using helium-neon laser (Melles Griot) with 543.5-nm wavelength and output power equal to 5 mW. The laser power was reduced using set of ND filters when illuminating a sample.

V. SIMULATION SECTION

To simulate the PSCs, we have decided to apply the self-developed electrical drift-diffusion simulation tool. Using the continuity equations for electrons and holes, it describes quantitatively the mechanisms of the generation, the transport and the recombination of charge-carrier processes:

$$\frac{\partial n}{\partial t} = G - R_{\rm m} - R_{\rm b} - R_{\rm t} + \frac{1}{a} \nabla \cdot J_n,\tag{1}$$

$$\frac{\partial p}{\partial t} = G - R_{\rm m} - R_{\rm b} - R_{\rm t} - \frac{1}{q} \nabla \cdot J_p, \tag{2}$$

where n and p represent the concentrations of electron and hole charge carriers, respectively. G denotes generation, R_m stands for trap-assisted recombination, R_b indicates radiative recombination, and R_t refers to the Auger recombination mechanism. Additionally, q is the elementary charge, while J_n and J_p are the drift-diffusion currents for electrons and holes, respectively. Both charge-carrier concentrations are linked through the Poisson equation, which calculates the electric potential arising from free charge carriers:

$$\nabla \cdot F = \frac{q}{\epsilon_0 \epsilon_r} (p - n + N_D - N_A), \tag{3}$$

where ϵ_0 is the vacuum permittivity, ϵ_r describes the material's permittivity, and N_D and N_A denote the concentrations of donor and acceptor impurities, respectively. A more detailed description is available in our previous work [53]. The transient trap, modified Langevin, and the

Auger effects are considered the dominant recombination processes in the simulated devices. To define the transient traps in conduction band (c) and valence band (v) we used time-dependent occupancy of traps

$$\frac{\partial n_t}{\partial t} = R_{\rm nc} - R_{\rm pc},\tag{4}$$

$$\frac{\partial p_t}{\partial t} = R_{\rm pv} - R_{\rm nv},\tag{5}$$

with recombination rates

$$R_{\rm nc} = C_{\rm nc}(n(N_{\rm tc} - n_t) - n_1 \times n_t),$$
 (6)

$$R_{\rm nv} = C_{\rm nv}(n \times p_t - n_1(N_{\rm tv} - p_t)),$$
 (7)

$$R_{\rm pc} = C_{\rm pc}(p \times n_t - p_1(N_{\rm tc} - n_t)),$$
 (8)

$$R_{\rm pv} = C_{\rm pv}(p(N_{\rm tv} - p_t) - p_1 \times p_t).$$
 (9)

where $C_{n(p)c}$ and $C_{n(p)v}$ is an electron (a hole) capture rates for holes in conduction and valence band, N_{tc} and N_{tv} represents the density of defect states for conduction and valence band, and the parameters n_1 and p_1 are given by

$$n_1 = N_c \exp\left(-\frac{E_c - E_t}{k_B T}\right),\tag{10}$$

$$p_1 = N_v \exp\left(-\frac{E_t - E_v}{k_B T}\right),\tag{11}$$

where N_c and N_v are the effective densities of states, E_c and E_v represent the conduction and valence band edges (energies), respectively, and E_t is a trap energy level situated in the midpoint of the band gap (E_g) . The energy alignment between layers in a solar cell was analyzed using the generalized potential technique, as detailed in prior studies [54,55]. Interface recombination was modeled by incorporating an additional perovskite layer, identical in all electrical parameters except for defect density of states (N_t) , as outlined in our previous work [53]. The bandbending effect was replicated using multiple perovskite layers, adjusting only the energy levels (conduction and valence band) to simulate the exponential energy-bending effect, similar to our previous studies [48]. We applied Schottky contacts as boundary conditions on both sides. The model includes spatial boundary conditions specified for electron and hole concentrations, electric potential, and the currents of both carriers. At t = 0, zero values are assumed for all variables. For charge-carrier concentrations, differences are noted at the top (x = L) and bottom

(x = 0) electrodes, which leads to

$$n(0) = N_c \exp\left(\frac{-\phi_n}{k_B T}\right), \quad p(0) = N_v \exp\left(\frac{\phi_n - E_g}{k_B T}\right),$$
(12)

$$n(L) = N_c \exp\left(\frac{\phi_p - E_g}{k_B T}\right), \quad p(L) = N_v \exp\left(\frac{-\phi_p}{k_B T}\right),$$
(13)

where ϕ_n and ϕ_p are work functions for both electrodes. The boundary conditions for the electric potential are established by

$$\phi(0) = V_{\text{built}} - V_a, \quad \phi(L) = 0.$$
 (14)

The built-in voltage (V_{built}) and the applied voltage (V_a) are defined as follows.

Ion mobilities in the perovskite layer are usually in the range of 10^{-7} to 10^{-6} cm² V⁻¹ s⁻¹ [56]. Figure S12 within the Supplemental Material [44] shows that the ion mobility has negligible impact on the TPC simulations for the mobilities in the range of 10^{-8} to 10^{-6} cm² V⁻¹ s⁻¹. Therefore, the migration of ions is neglected in our studies due to the negligible effect on the operation of PSCs in the studied timescale. The Scharfetter-Gummel discretization method with the Chebyshev polynomials was used for the electrical model. The energy alignment between layers in a solar cell was considered using the generalized potentials technique. To find a global minimum and avoid local optimizations for the numerical solution in the fitting procedure we have used the differential evolution algorithm [57]. Subsequently, we enhanced the accuracy of this global minimum by applying the Nelder-Mead model [58,59]. The chi-square test was used to determine the mismatch between simulation data and experimental results. It uses the R^2 value from regression analysis, which ranges from 0% to 100% to determine how well the simulation data fit the experimental results. All simulations were performed using our own numerical code written in C++ and python.

The simulation was divided into two main steps. At the outset, simulations were performed for the J-V characteristics under steady-state conditions for Cs-Br first, and then for Pb-Br. In the second step transient photocurrent was analyzed, once again starting with Cs-Br and moving to Pb-Br. The regular parameters used in simulations are presented in Table S1 (Supplemental Material [44]).

ACKNOWLEDGMENT

This research was funded in part by National Science Centre, in cooperation with the M-ERA.NET 3 Call 2021 for the Grant No. 2021/03/Y/ST5/00233. This project has received funding from the European Union's Horizon 2020 research and innovation program under Grant Agreement

No 958174. Calculations were carried out at the Academic Computer Centre (CI TASK) in Gdansk.

- [1] National Renewable Energy Laboratory (NREL), Chart of Best Research-Cell Efficiencies, https://www.nrel.gov/pv/ assets/images/efficiency-chart.png (accessed 2024-02-24).
- [2] W. E. I. Sha, X. Ren, L. Chen, and W. C. H. Choy, The efficiency limit of CH₃NH₃PbI₃ perovskite solar cells, Appl. Phys. Lett. 106, 221104 (2015).
- [3] T. S. Sherkar, C. Momblona, L. Gil-Escrig, J. Ávila, M. Sessolo, H. J. Bolink, and L. J. A. Koster, Recombination in perovskite solar cells: Significance of grain boundaries, interface traps, and defect ions, ACS Energy Lett. 2, 1214 (2017).
- [4] K. L. Chen, Optoelectronic techniques boost the investigation on hysteresis and ion migration in perovskite photovoltaics, J. Phys.: Conf. Ser. 2386, 012050 (2022).
- [5] S. Srivastava, S. Ranjan, L. Yadav, T. Sharma, S. Choudhary, D. Agarwal, A. Singh, S. Satapathi, R. K. Gupta, A. Garg, and K. S. Nalwa, Advanced spectroscopic techniques for characterizing defects in perovskite solar cells, Commun. Mater. 4, 52 (2023).
- [6] B. Romero, S. Delgado, D. Glowienka, C.-T. Chang, G. D. Pozo, B. Arredondo, D. Martín-Martín, P. Contreras, and Y. Galagan, Highly stable CsFaPbIBr perovskite solar cells with dominant bulk recombination at real operating temperatures, Sustainable Energy Fuels 7, 2146 (2023).
- [7] D. Glowienka and Y. Galagan, Light intensity analysis of photovoltaic parameters for perovskite solar cells, Adv. Mater. 34, 2105920 (2022).
- [8] X. Chen, Y. Shirai, M. Yanagida, and K. Miyano, Photocarrier dynamics in perovskite-based solar cells revealed by intensity-modulated photovoltage spectroscopy, Phys. Chem. Chem. Phys. 20, 17918 (2018).
- [9] P. Srivastava, R. Kumar, H. Ronchiya, and M. Bag, Intensity modulated photocurrent spectroscopy to investigate hidden kinetics at hybrid perovskite–electrolyte interface, Sci. Rep. 12, 14212 (2022).
- [10] A. Bou, H. Abolinš, A. Ashoka, H. Cruanyes, A. Guerrero, F. Deschler, and J. Bisquert, Extracting in situ charge carrier diffusion parameters in perovskite solar cells with light modulated techniques, ACS Energy Lett. 6, 2248 (2021).
- [11] S. Ravishankar, C. Aranda, S. Sanchez, J. Bisquert, M. Saliba, and G. Garcia-Belmonte, Perovskite solar cell modeling using light- and voltage-modulated techniques, J. Phys. Chem. C 123, 6444 (2019).
- [12] S. Ravishankar, A. Riquelme, S. K. Sarkar, M. Garcia-Batlle, G. Garcia-Belmonte, and J. Bisquert, Intensity-modulated photocurrent spectroscopy and its application to perovskite solar cells, J. Phys. Chem. C 123, 24995 (2019).
- [13] N. Parikh, S. Narayanan, H. Kumari, D. Prochowicz, A. Kalam, S. Satapathi, S. Akin, M. M. Tavakoli, and P. Yadav, Recent progress of light intensity-modulated small perturbation techniques in perovskite solar cells, Phys. Status Solidi (RRL)—Rapid Res. Lett. 16, 2100510 (2022).
- [14] A. Guerrero, J. Bisquert, and G. Garcia-Belmonte, Impedance spectroscopy of metal halide perovskite solar

- cells from the perspective of equivalent circuits, Chem. Rev. **121**, 14430 (2021).
- [15] A. Pockett, G. E. Eperon, T. Peltola, H. J. Snaith, A. Walker, L. M. Peter, and P. J. Cameron, Characterization of planar lead halide perovskite solar cells by impedance spectroscopy, open-circuit photovoltage decay, and intensity-modulated photovoltage/photocurrent spectroscopy, J. Phys. Chem. C 119, 3456 (2015).
- [16] E. Ghahremanirad, O. Almora, S. Suresh, A. A. Drew, T. H. Chowdhury, and A. R. Uhl, Beyond protocols: Understanding the electrical behavior of perovskite solar cells by impedance spectroscopy, Adv. Energy Mater. 13, 2204370 (2023).
- [17] E. Guillén, F. J. Ramos, J. A. Anta, and S. Ahmad, Elucidating transport-recombination mechanisms in perovskite solar cells by small-perturbation techniques, J. Phys. Chem. C 118, 22913 (2014).
- [18] D. Pitarch-Tena, T. T. Ngo, M. Vallés-Pelarda, T. Pauporté, and I. Mora-Seró, Impedance spectroscopy measurements in perovskite solar cells: Device stability and noise reduction, ACS Energy Lett. 3, 1044 (2018).
- [19] E. Palomares, N. F. Montcada, M. Méndez, J. Jiménez-López, W. Yang, and G. Boschloo, in *Characterization Techniques for Perovskite Solar Cell Materials*, edited by M. Pazoki, A. Hagfeldt, and T. Edvinsson, Micro and Nano Technologies (Elsevier, 2020), pp. 161–180.
- [20] L. Krückemeier, B. Krogmeier, Z. Liu, U. Rau, and T. Kirchartz, Understanding transient photoluminescence in halide perovskite layer stacks and solar cells, Adv. Energy Mater. 11, 2003489 (2021).
- [21] S. Wheeler, D. Bryant, J. Troughton, T. Kirchartz, T. Watson, J. Nelson, and J. R. Durrant, Transient opto-electronic analysis of the impact of material energetics and recombination kinetics on the open-circuit voltage of hybrid perovskite solar cells, J. Phys. Chem. C 121, 13496 (2017).
- [22] Z. S. Wang, F. Ebadi, B. Carlsen, W. C. H. Choy, and W. Tress, Transient photovoltage measurements on perovskite solar cells with varied defect concentrations and inhomogeneous recombination rates, Small Methods 4, 2000290 (2020).
- [23] M.-C. Kim, S.-Y. Ham, D. Cheng, T. A. Wynn, H. S. Jung, and Y. S. Meng, Advanced characterization techniques for overcoming challenges of perovskite solar cell materials, Adv. Energy Mater. 11, 2001753 (2021).
- [24] E. J. Juarez-Perez, R. S. Sanchez, L. Badia, G. Garcia-Belmonte, Y. S. Kang, I. Mora-Sero, and J. Bisquert, Photoinduced giant dielectric constant in lead halide perovskite solar cells, J. Phys. Chem. Lett. 5, 2390 (2014).
- [25] N. Aristidou, C. Eames, I. Sanchez-Molina, X. Bu, J. Kosco, M. S. Islam, and S. A. Haque, Fast oxygen diffusion and iodide defects mediate oxygen-induced degradation of perovskite solar cells, Nat. Commun. 8, 15218 (2017).
- [26] H.-S. Kim, I.-H. Jang, N. Ahn, M. Choi, A. Guerrero, J. Bisquert, and N.-G. Park, Control of *I–V* hysteresis in CH₃NH₃PbI₃ perovskite solar cell, J. Phys. Chem. Lett. 6, 4633 (2015).
- [27] P. Calado, A. M. Telford, D. Bryant, X. Li, J. Nelson, B. C. O'Regan, and P. R. Barnes, Evidence for ion migration in

- hybrid perovskite solar cells with minimal hysteresis, Nat. Commun. 7, 13831 (2016).
- [28] M. De Bastiani, G. Dell'Erba, M. Gandini, V. D'Innocenzo, S. Neutzner, A. R. S. Kandada, G. Grancini, M. Binda, M. Prato, J. M. Ball, M. Caironi, and A. Petrozza, Ion migration and the role of preconditioning cycles in the stabilization of the *J-V* characteristics of inverted hybrid perovskite solar cells, Adv. Energy Mater. 6, 1501453 (2016).
- [29] C. Eames, J. M. Frost, P. R. F. Barnes, B. C. O'Regan, A. Walsh, and M. S. Islam, Ionic transport in hybrid lead iodide perovskite solar cells, Nat. Commun. 6, 7497 (2015).
- [30] P. Basumatary and P. Agarwal, Photocurrent transient measurements in MAPbI₃ thin films, J. Mater. Sci.: Mater. Electron. 31, 10047 (2020).
- [31] L. Li, P. Jia, W. Bi, Y. Tang, B. Song, L. Qin, Z. Lou, Y. Hu, F. Teng, and Y. Hou, Impacts of carrier trapping and ion migration on charge transport of perovskite solar cells with TiO_x electron transport layer, RSC Adv. 10, 28083 (2020).
- [32] J. Shi, D. Li, Y. Luo, H. Wu, and Q. Meng, Opto-electro-modulated transient photovoltage and photocurrent system for investigation of charge transport and recombination in solar cells, Rev. Sci. Instrum. 87, 123107 (2016).
- [33] J. Shi, Y. Li, Y. Li, D. Li, Y. Luo, H. Wu, and Q. Meng, From ultrafast to ultraslow: Charge-carrier dynamics of perovskite solar cells, Joule 2, 879 (2018).
- [34] M. T. Neukom, A. Schiller, S. Züfle, E. Knapp, J. Ávila, D. Pérez-del Rey, C. Dreessen, K. P. Zanoni, M. Sessolo, H. J. Bolink, and B. Ruhstaller, Consistent device simulation model describing perovskite solar cells in steady-state, transient, and frequency domain, ACS Appl. Mater. Interfaces 11, 23320 (2019).
- [35] M. De Bastiani, E. Aydin, T. Allen, D. Walter, A. Fell, J. Peng, N. Gasparini, J. Troughton, D. Baran, K. Weber, T. P. White, and S. De Wolf, Interfacial dynamics and contact passivation in perovskite solar cells, Adv. Electron. Mater. 5, 1800500 (2019).
- [36] J. Shi, X. Xu, H. Zhang, Y. Luo, D. Li, and Q. Meng, Intrinsic slow charge response in the perovskite solar cells: Electron and ion transport, Appl. Phys. Lett. **107**, 163901 (2015).
- [37] C. R. McNeill, I. Hwang, and N. C. Greenham, Photocurrent transients in all-polymer solar cells: Trapping and detrapping effects, J. Appl. Phys. 106, 024507 (2009).
- [38] N. S. Christ, S. W. Kettlitz, S. Valouch, S. Züfle, C. Gärtner, M. Punke, and U. Lemmer, Nanosecond response of organic solar cells and photodetectors, J. Appl. Phys. 105, 104513 (2009).
- [39] I. Hwang and N. C. Greenham, Modeling photocurrent transients in organic solar cells, Nanotechnology 19, 424012 (2008).
- [40] R. A. Belisle, W. H. Nguyen, A. R. Bowring, P. Calado, X. Li, S. J. C. Irvine, M. D. McGehee, P. R. F. Barnes, and B. C. O'Regan, Interpretation of inverted photocurrent transients in organic lead halide perovskite solar cells: Proof of the field screening by mobile ions and determination of the space charge layer widths, Energy Environ. Sci. 10, 192 (2017).

- [41] S. Mabrouk, A. Dubey, W. Zhang, N. Adhikari, B. Bahrami, M. N. Hasan, S. Yang, and Q. Qiao, Increased efficiency for perovskite photovoltaics via doping the PbI₂ layer, J. Phys. Chem. C 120, 24577 (2016).
- [42] R. Hidayat, A. A. Nurunnizar, A. Fariz, Herman, E. S. Rosa, Shobih, T. Oizumi, A. Fujii, and M. Ozaki, Revealing the charge carrier kinetics in perovskite solar cells affected by mesoscopic structures and defect states from simple transient photovoltage measurements, Sci. Rep. 10, 19197 (2020).
- [43] D. Głowienka, F. Di Giacomo, M. Najafi, I. Dogan, A. Mameli, F. J. M. Colberts, J. Szmytkowski, and Y. Galagan, Effect of different bromine sources on the dual cation mixed halide perovskite solar cells, ACS Appl. Energy Mater. 3, 8285 (2020).
- [44] See Supplemental Material at http://link.aps.org/supplemental/10.1103/PhysRevApplied.22.054025 for Table S1 and Figures S1—S12. The Supplemental Material provides additional data, including a list of common parameters used in drift-diffusion simulations, and both experimental and simulated *J-V* and TPC results for understanding the losses in PSCs. Also, the statistical distribution of photovoltaic parameters, along EQE and MPP measurements are included.
- [45] J. Wang, X. Ren, S. Shi, C. Leung, and P. K. Chan, Charge accumulation induced S-shape *J-V* curves in bilayer heterojunction organic solar cells, Org. Electron. 12, 880 (2011).
- [46] J. Szmytkowski, Y. Galagan, and D. Glowienka, Exploring the interfacial effects at the ETL/perovskite boundary in the semitransparent perovskite solar cells, Solar Energy 266, 112176 (2023).
- [47] L. M. Herz, Charge-carrier mobilities in metal halide perovskites: Fundamental mechanisms and limits, ACS Energy Lett. 2, 1539 (2017).
- [48] D. Glowienka, S.-H. Huang, P.-H. Lee, F.-Y. Tsai, and W.-F. Su, Understanding the dominant physics mechanisms on the *p-i-n* perovskite solar cells fabricated by scalable slot-die coating process in ambient air, Solar RRL **8**, 2300791 (2024).
- [49] S. D. Stranks, G. E. Eperon, G. Grancini, C. Menelaou, M. J. P. Alcocer, T. Leijtens, L. M. Herz, A. Petrozza, and H. J. Snaith, Electron-hole diffusion lengths exceeding 1 μm in

- an organometal trihalide perovskite absorber, Science **342**, 341 (2013).
- [50] A. Mahapatra, V. Anilkumar, J. Nawrocki, S. V. Pandey, R. D. Chavan, P. Yadav, and D. Prochowicz, Transient photocurrent response in a perovskite single crystal-based photodetector: A case study on the role of electrode spacing and bias, Adv. Electron. Mater. 9, 2300226 (2023).
- [51] W. Tress, M. Yavari, K. Domanski, P. Yadav, B. Niesen, J. P. Correa Baena, A. Hagfeldt, and M. Graetzel, Interpretation and evolution of open-circuit voltage, recombination, ideality factor and subgap defect states during reversible light-soaking and irreversible degradation of perovskite solar cells, Energy Environ. Sci. 11, 151 (2018).
- [52] A. Babayigit, J. D'Haen, H.-G. Boyen, and B. Conings, Gas quenching for perovskite thin film deposition, Joule 2, 1205 (2018).
- [53] D. Głowienka, D. Zhang, F. Di Giacomo, M. Najafi, S. Veenstra, J. Szmytkowski, and Y. Galagan, Role of surface recombination in perovskite solar cells at the interface of HTL/CH₃NH₃PbI₃, Nano Energy 67, 104186 (2020).
- [54] M. Lundstrom and R. Schuelke, Numerical analysis of heterostructure semiconductor devices, IEEE Trans. Electron. Devices **30**, 1151 (1983).
- [55] M. Gruber, B. Stickler, G. Trimmel, F. Schürrer, and K. Zojer, Impact of energy alignment and morphology on the efficiency in inorganic—organic hybrid solar cells, Org. Electron. 11, 1999 (2010).
- [56] M. García-Batlle, S. Deumel, J. E. Huerdler, S. F. Tedde, O. Almora, and G. Garcia-Belmonte, Effective ion mobility and long-term dark current of metal halide perovskites with different crystallinities and compositions, Adv. Photonics Res. 3, 2200136 (2022).
- [57] M. Georgioudakis and V. Plevris, A comparative study of differential evolution variants in constrained structural optimization, Front. Built Environ. 6, 102 (2020).
- [58] J. A. Nelder and R. Mead, A simplex method for function minimization, Comput. J. 7, 308 (1965).
- [59] M. Newville, T. Stensitzki, D. B. Allen, M. Rawlik, A. Ingargiola, and A. Nelson, Lmfit: Non-linear leastsquare minimization and curve-fitting for python, Astrophysics Source Code Library, record ascl:1606.014 (2016), https://ui.adsabs.harvard.edu/abs/2016ascl.soft06014N.